ACS NANO

www.acsnano.org

Rare-Earth Iron Garnet Superlattices with Sub-unit Cell Composition Modulation

Bharat Khurana, Allison C. Kaczmarek, Chung-Tao Chou, Tingyu Su, Katharina Lasinger, Tomas Grossmark, David C. Bono, Luqiao Liu, and Caroline A. Ross*

Cite This: https://doi.org/10.1021/acsnano.4c11117 Read Online

ACCESS | Metrics & More | Article Recommendations | Supporting Information

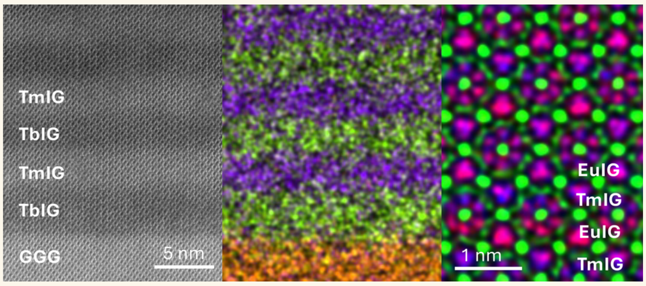

ABSTRACT: Oxide superlattices reveal a rich array of emergent properties derived from the composition modulation and the resulting lattice distortion, charge transfer, and symmetry reduction that occur at the interfaces between the layers. The great majority of studies have focused on perovskite oxide superlattices, revealing, for example, the appearance of an interfacial 2D electron gas, magnetic moment, or improper ferroelectric polarization that is not present in the parent phases. Garnets possess greater structural complexity than perovskites: the cubic garnet unit cell contains 160 atoms with the cations distributed between three different coordination sites, and garnets exhibit a wide range of useful properties, including ferrimagnetism and ion transport. However, there have been few reports of the synthesis or properties of garnet superlattices, with layer thicknesses approaching the unit cell dimension of 1.2 nm. Here, we describe superlattices made from Bi and rare earth (RE = Tm, Tb, Eu, Lu) iron garnets (IGs) grown by pulsed laser deposition. Atom probe tomography and transmission electron microscopy reveal the composition modulation without dislocations and layer thicknesses as low as 0.45 nm, less than half a unit cell. TmIG/TbIG superlattices exhibit perpendicular magnetic anisotropy that is qualitatively different from the in-plane anisotropy of the solid solution, and BiIG/LuIG superlattices exhibit ferromagnetic resonance linewidth characteristics of the end-members rather than the solid solution. Garnet superlattices provide a playground for exploring interface physics within the vast parameter space of cation coordination and substitution.

KEYWORDS: *iron garnet, superlattice, multilayer, ferrimagnet, magnetic anisotropy, pulsed laser deposition*

Complex oxide heterostructures exhibit fascinating emergent phenomena driven by broken symmetry, structural distortions, and charge transfer that occur at oxide interfaces. Examples include the 2D electron gases or magnetic moments that appear at interfaces between otherwise insulating and nonmagnetic perovskites $LaAlO_3$ and $SrTiO_3$,[1] improper ferroelectricity in $PbTiO_3/SrTiO_3$ perovskite superlattices,[2] anomalous spin-glass transitions in superlattices of magnetically frustrated $ZnCr_2O_4/ZnFe_2O_4$ spinels,[3] and metallicity in rutile-structured TiO_2/IrO_2 superlattices.[4] Garnets, with formula $A_3B_2C_3O_{12}$, have three different types of cation sites in the b.c.c. unit cell, enabling an even greater range of compositional variation than in perovskites, ABO_3. Moreover, iron garnets in particular ($A_3Fe_5O_{12}$), are ferrimagnetic insulators with a high Curie temperature of 560 K, and their magneto-optical properties, low damping, and high domain wall velocities make them essential components in a range of microwave, magnetic, and photonic devices.[5−7] Other garnets have applications in lasing materials (e.g., aluminum garnets) and as ionic conductors (Li-stuffed garnets).[8−10]

In rare earth iron garnets ($RE_3Fe_5O_{12}$, REIG), the RE ion has fundamental importance in determining the magnetic anisotropy, magnetostriction, magnetic moment, compensation temperature, damping, and optical properties of the garnet.[11−13] As a perovskite analogy, in rare earth nickelates ($RENiO_3$), changing the RE leads to a dramatic change in electronic and magnetic properties,[14] and in rare earth orthoferrites ($REFeO_3$), the RE determines the Néel temperature and spin reorientation of the Fe sublattice and drives improper ferroelectricity.[15−18] A variety of studies have demonstrated the growth of perovskites and spinel superlattices,[3,19−23] including orthoferrite or nickelate superlattices

Received: August 13, 2024
Revised: November 20, 2024
Accepted: November 27, 2024

ACS Publications

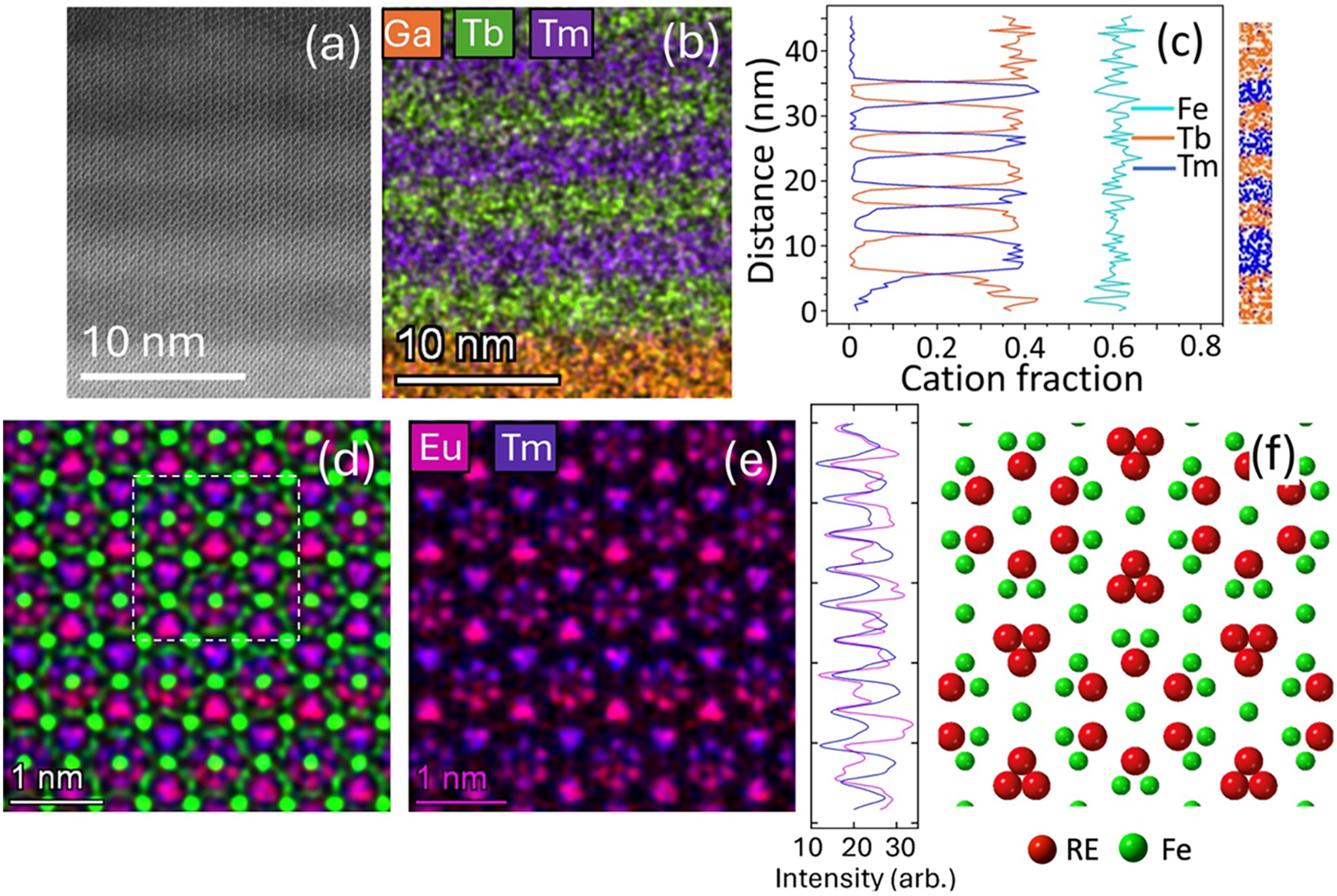

Figure 1. Superlattice garnet films. (a) HAADF image for a cross-section of a (TbIG/TmIG)/(111) GGG superlattice with 2.8 nm thick layers along the [$1\bar{1}0$] zone axis. (b) TEM EDS map for the sample in panel (a). (c) Projected 2D image for APT data for a (TbIG/TmIG)/(111) GGG multilayered film with different layer thicknesses of TbIG and TmIG. In the adjacent image, each dot represents the position of the ion detected by mass spectrometry. (d, e) Elemental maps of a superlattice of EuIG−TmIG grown on a (110) substrate imaged along the [$\bar{1}11$] in-plane zone axis. They show the same area with Eu in magneta and Tm in purple, but panel (d) includes Fe. The plot adjacent to panel (e) shows the integrated intensity of Eu and Tm. (f) Crystal structure of REIG along the [111] zone axis showing the Fe (green) and RE (red) sites, matching the arrangement seen in the dashed square in panel (d).

with intriguing properties.[24−26] Therefore, we might expect RE garnet superlattices to provide a rich opportunity for materials engineering, where interfacial strain, composition gradients, and the loss of inversion symmetry could drive piezomagnetic[27] or flexomagnetic[28,29] effects, growth-induced anisotropy,[30,31] Dzyaloshinskii−Moriya interactions, or a ferroelectric response.[32]

Despite the exceptional properties of garnets and the opportunities inherent in interface engineering, there has been little study of garnet heterostructures and multilayers. Garnet multilayers of $Y_3Fe_5O_{12}/Bi_3Fe_5O_{12}$ (YIG/BiIG), YIG/$(EuBi)_3Fe_5O_{12}$, YIG/$Gd_3Fe_5O_{12}$, and $(Bi,Dy)_3(Fe,Ga)_5O_{12}/(Bi,Lu)_3(Fe,Al)_5O_{12}$ with layer thicknesses of tens to hundreds of nanometers were synthesized for magneto-optical and optical applications, such as Bragg reflectors.[33−36] The study of garnet superlattices with nm-scale layer thicknesses is restricted to YIG/$Gd_3Ga_5O_{12}$ (GGG) with a minimum layer thickness of one unit cell (cubic lattice parameter a = 1.2 nm),[37] GGG/$Gd_3Sc_2Ga_3O_{12}$ (GSGG) with layers of ∼2 nm,[23] and YIG/GGG/$Ca_3Sc_2Si_2TiO_{12}$ with each layer 3.5 nm thick.[21,38−41] Structural characterization is limited, and the only magnetic component is YIG.

Here, we describe the structure and magnetic properties of coherent superlattices made from terbium iron garnet (TbIG, $Tb_3Fe_5O_{12}$), europium iron garnet (EuIG, $Eu_3Fe_5O_{12}$), thulium iron garnet (TmIG, $Tm_3Fe_5O_{12}$), lutetium iron garnet (LuIG, $Lu_3Fe_5O_{12}$), and bismuth iron garnet (BiIG). TbIG, EuIG, and TmIG were selected due to their diverse magnetostriction and lattice parameters, whereas, in LuIG and BiIG, the dodecahedral cation is nonmagnetic, and LuIG has very low damping similar to YIG. Unlike prior work, all layers are ferrimagnetic, and the composition modulation involves only the dodecahedral sites. Compositionally modulated layers of 0.45 nm thickness, half the out-of-plane lattice spacing, are confirmed both by elemental analysis of a EuIG/TmIG superlattice and from the magnetic anisotropy of a TbIG/TmIG superlattice, which differs qualitatively from that of the solid solution $(Tb_{0.5}Tm_{0.5})_3Fe_5O_{12}$. LuIG/BiIG superlattices exhibit ferromagnetic resonance (FMR) linewidth characteristics of the end-member BiIG and not the solid solution. These findings demonstrate the engineering of garnet multilayers with layering at a sub-unit cell scale, providing opportunities to explore interfacial phenomena in iron garnets with tunable magnetic and spintronic properties.

RESULTS AND DISCUSSION

The superlattices in this study, summarized in Table S1, Supporting Information (Supplementary Note 1), were

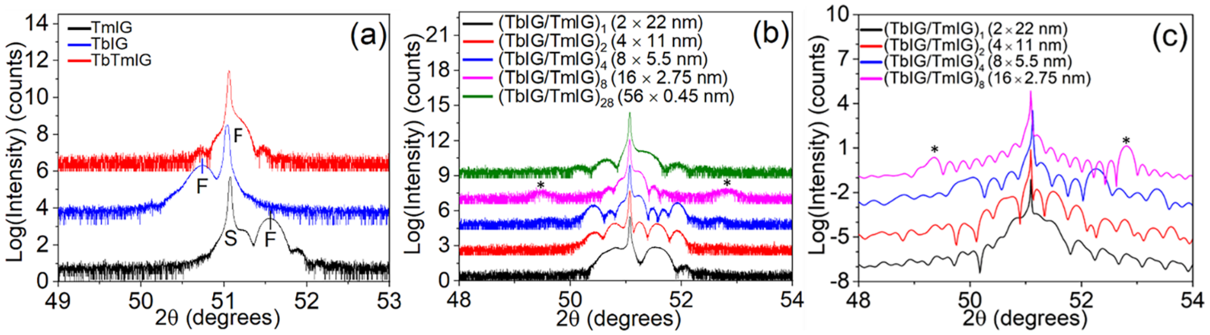

Figure 2. X-ray diffraction scans of garnet films. (a) HRXRD scans of TmIG, TbIG, and TbTmIG films deposited on (111) GGG substrates, vertically offset for clarity with film and substrate peaks labeled F and S, respectively. (b) HRXRD scans of bilayered, 4-layered, 8-layered, 16-layered, and 56-layered films of (TbIG/TmIG)/(111) GGG vertically offset for clarity. (c) Simulation of XRD scans for bilayered, 4-layered, 8-layered, and 16-layered films of (TbIG/TmIG)/(111) GGG with a total thickness of 44 nm. Satellite peaks from the multilayer with 2.75 nm thick layers are indicated in (b, c) with a star.

deposited by pulsed laser deposition (PLD) on GGG and GSGG substrates at oxygen pressures of 50−150 mTorr, a substrate temperature of 650 °C (750 °C for TmIG/EuIG), and a laser repetition rate of 10 Hz (see the Methods section). Superlattices with a total thickness of 15−44 nm, consisting of 2−56 individual layers, were formed by ablation from targets of the end-members (TbIG, TmIG, EuIG, LuIG, BiIG) based on the deposition rate established from each target. In contrast, a substitutional solid solution film, $(Tb_{0.5}Tm_{0.5})_3Fe_5O_{12}$ (TbTmIG) or $(Lu_{0.5}Bi_{0.5})_3Fe_5O_{12}$ (LuBiIG), was formed when the number of shots per layer is low enough to allow intermixing of the species on the c sites.

Figure 1 reveals direct evidence of superlattice formation from transmission electron microscopy (TEM) high-angle annular dark-field (HAADF) imaging and 3D atom probe tomography (APT). A cross-section of the 44 nm thick, 16-layered TbIG/TmIG film on (111) GGG and its energy-dispersive spectroscopy (EDS) map (Figures 1a,b and Supplementary Note 2) reveal a coherent, compositionally modulated superlattice with a layer thickness of 2.8 nm, in which the transition between the layers occurs within an interfacial width of less than 1 nm. No dislocations are present within the image area, and the film is fully strained to the substrate, consistent with the coherent epitaxial growth of a variety of single-layer iron garnet films with thicknesses of up to 90 nm on garnet substrates.[42,43] A separate TbIG/TmIG sample made with various layer thicknesses analyzed via APT (Figure 1c, Methods) also shows interface widths below 1 nm. The RE:Fe cation stoichiometry was close to its bulk value of 3:5 for TbIG and TmIG layers of 4.5 and 3.2 nm, respectively (Supplementary Note 1). To illustrate superlattice formation for another pair of REIGs and on a different substrate orientation, we imaged a TmIG/EuIG film on (110) GGG (Figure 1d,e), along the $[\bar{1}11]$ in-plane zone axis. It exhibits compositionally modulated layers of 0.45 nm thickness, half the out-of-plane spacing of $a/\sqrt{2}$.

TEM and APT, as well as atomic force microscopy (AFM) (Supplementary Notes 2, 3) show that while multilayers initially grow with a smooth surface (e.g., r.m.s. roughness of 0.2 nm for a 15 nm thick film, Figure S4b), roughness develops in multilayers grown at 150 mTorr when the thickness exceeds ∼25 nm, Figure S4a, corresponding to waviness in the compositionally modulated layers. Roughness was suppressed by growing the films at 50 mTorr (Figure S4c), suggesting that it is promoted by the lower mobility conditions present during deposition at high oxygen pressures.

Considering the in-plane lattice match to the substrate, symmetric high-resolution X-ray diffraction (HRXRD) scans of single-layer films TbIG, TmIG, and TbTmIG, Figure 2a, show that the TbIG is under in-plane compressive strain and the TmIG under tension, whereas the TbTmIG displays little strain. For a multilayer film consisting of thick layers, e.g., 22 nm, the HRXRD scans (Figure 2b and Supporting Information, Part 4) resemble a superposition of peaks corresponding to the single-layer TbIG and TmIG films. However, for multilayer films consisting of thinner layers, multiple peaks occur at positions different from those of the end-member peaks, including satellite peaks on either side of the main peak. XRD modeling of TbIG/TmIG multilayers with a finite number of layers, Figure 2c, yields good agreement with the measured data, further supporting the existence of a superlattice. Multilayer films made at lower oxygen pressures exhibit more prominent fringes, indicating reduced roughness and greater thickness uniformity (Figure S7).

Hysteresis loops from vibrating sample magnetometry (VSM), Figure 3 and Supplementary Note 5 show an out-of-plane easy axis for the TbIG and TmIG films and the TbIG/TmIG superlattices on (111) GGG substrates, whereas the solid solution TbTmIG film and superlattices grown on (100)-oriented GGG and (111)-oriented GSGG have an in-plane easy axis. To analyze these differences, we consider the net anisotropy, K_{eff}, defined as the difference in energy between the magnetization being oriented in-plane vs out-of-plane. Based on an expression for (111)-oriented iron garnet films,[30,42,43] the effective anisotropy is given by

$$K_{\text{eff}} = \frac{-K_1}{12} - \frac{\mu_0}{2}M_s^2 + \frac{9}{4}c_{44}\lambda_{111}\left(\frac{\pi}{2} - \beta\right) + K_G + K_I \tag{1}$$

Here, K_1 is the first-order cubic magnetocrystalline anisotropy constant, which is small compared to other terms (of order -100 J/m^3 for TbIG and TmIG); M_s is the saturation magnetization of the film, c_{44} is the shear modulus of the film, λ_{111} is the magnetostriction coefficient along <111>, β is the corner angle of the rhombohedrally distorted unit cell, K_G is the uniaxial growth-induced anisotropy,[30,44,45] originating from the preferential occupancy of cations or vacancies in nonequivalent sites. We include a term K_I to capture any

https://doi.org/10.1021/acsnano.4c11117

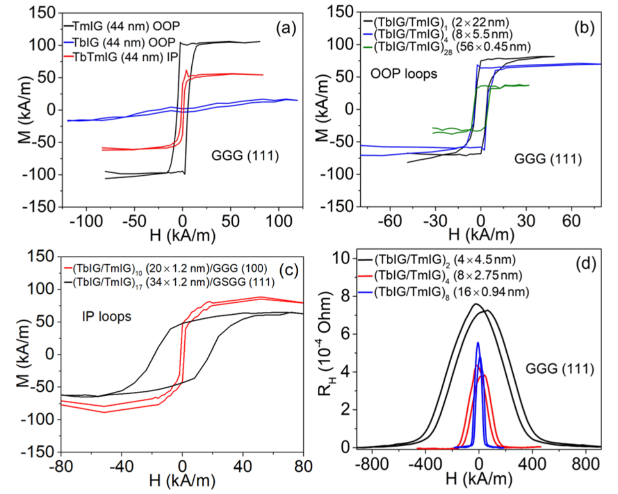

Figure 3. **(a) Hysteresis loops measured by VSM of TmIG, TbIG, and TbTmIG films deposited on the (111) GGG substrates. (b) VSM hysteresis loops of 2-, 8-, and 56-layered (TbIG/TmIG)/(111) GGG. (c) VSM hysteresis loops of 20-layered (TbIG/TmIG) deposited on (100) GGG and 34-layered (TbIG/TmIG) deposited on (111) GSGG. (d) In-plane SMR loops for 4-layered, 8-layered, and 16-layered (TbIG/TmIG)/(111) GGG.**

interfacial or surface contributions to anisotropy.[46,47] A positive K_{eff} results in an out-of-plane easy axis, i.e., perpendicular magnetic anisotropy (PMA).

The PMA of the TmIG film (in-plane tensile strain; $\lambda_{111} = -5.2 \times 10^{-6}$) and the TbIG film (in-plane compressive strain; $\lambda_{111} = +12 \times 10^{-6}$) on GGG substrates originates from their dominant magnetoelastic energy contributions.[48] In contrast, the TbTmIG solid solution film has little strain and an interpolated $\lambda_{111} = +3.4 \times 10^{-6}$; hence, the magnetoelastic energy term is small. Its in-plane easy axis indicates that any perpendicular growth-induced or surface anisotropy is insufficient to overcome the dominant shape anisotropy of $-\frac{\mu_0}{2}M_s^2$ for the TbTmIG solid solution. Therefore, the presence of PMA in the multilayer films is an indication that they are not intermixed but instead consist of layers that retain the magnetic characteristics of the end-members. In particular, the PMA of the 56-layered 25 nm thick TbIG/TmIG superlattice, which is qualitatively different from the in-plane easy axis of the TbTmIG solid solution, indicates that a composition modulation exists for TbIG/TmIG layers of 0.45 nm thickness.

Multilayers were also deposited onto other substrates: (111)-oriented GSGG, which has a larger lattice parameter than GGG, and (001)-oriented GGG. First, considering films on (111) GSGG, based on the strain state and magnetostriction, we expect an epitaxial TmIG film to have PMA but epitaxial TbIG and TbTmIG to have in-plane anisotropy. A TbIG/TmIG superlattice on (111) GSGG showed an in-plane easy axis (Figure 3c), which is consistent with its multilayer structure; however, it is also consistent with intermixing to form a solid solution TbTmIG (Supplementary Note 7). Next, for a film on a (100)-oriented substrate, analogously to eq 1, the anisotropy is given by[43]

$$K_{\mathrm{eff},100} = \frac{3}{2}\lambda_{100}(c_{11} - c_{12})(\varepsilon_{zz} - \varepsilon_{xx}) - \frac{\mu_0}{2}M_s^2 + K_G + K_I \tag{2}$$

where λ_{100} is the magnetostriction coefficient along <100>, c_{11} and c_{12} are elastic constants of the film material, and ε_{ii} denotes the *i*th normal strain component. The in-plane easy axis observed for the TbIG/TmIG superlattice on (100) GGG (Figure 3c) is consistent with the behavior expected from a multilayer and also with a solid solution (Supplementary Note 8). Therefore, unlike the (111) GGG substrate, neither (111) GSGG nor (100) GGG substrates enable us to distinguish between a TbIG/TmIG multilayer and a TbTmIG solid solution based solely on the orientation of the easy axis.

We quantify the anisotropy of the TbIG/TmIG/(111) GGG superlattices and TbTmIG/(111) GGG solid solution using spin Hall magnetoresistance (SMR) measurements of films of thicknesses below 22 nm with a root-mean-square roughness below 0.2 nm. A 4 nm thick Pt layer was sputtered onto the films and patterned into Hall crosses, and the anisotropy field H_K and net anisotropy $K_{\mathrm{eff}} = \mu_0 M_s H_K/2$ were determined from the SMR (see the Methods section). Figure 3d shows that the K_{eff} decreased as the layer thickness decreased from 13.8 ± 1.9 kJ/m^3 for 4.5 nm layers to 1.9 ± 0.3 J/m^3 for 0.94 nm layers, i.e., the PMA becomes weaker as the layers become thinner. We attribute this to the increasing volume fraction of the interfaces. The TbTmIG solid solution has an in-plane easy axis with $K_{\mathrm{eff}} = -3.8 \pm 0.3$ kJ/m^3, dominated by shape anisotropy of -2.1 ± 0.7 kJ/m^3. The interfacial regions of the superlattice with their intermediate composition are similarly expected to contribute an in-plane anisotropy, and a higher density of interfaces therefore lowers the net PMA of the superlattice.

We now turn to superlattices based on BiIG and LuIG, comparing single-layer films of BiIG, LuIG, and solid solution LuBiIG with a BiIG/LuIG multilayer with 2.9 nm layers on (111) GGG. While BiIG is not a stable phase in bulk, it crystallizes on a garnet substrate as an epitaxial thin film with a lattice parameter of 1.263 nm.[49] From XRD, Figures 4a and S6, epitaxial LuIG on GGG is in tension, whereas BiIG exhibits an

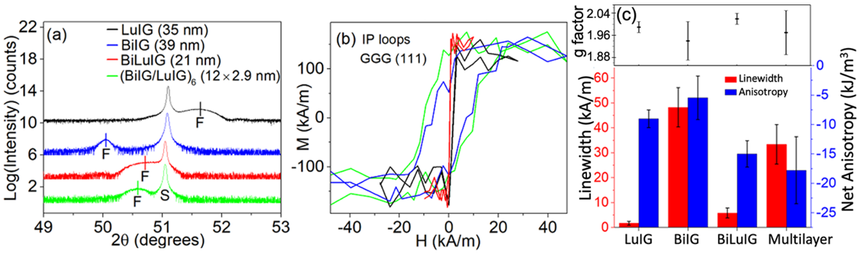

Figure 4. **(a) HRXRD scans of LuIG, BiIG, BiLuIG, and 12-layered BiIG/LuIG deposited on (111) GGG, vertically offset for clarity, with film and substrate peaks labeled F and S, respectively. (b) In-plane VSM hysteresis loops for the films in panel (a). (c) Landé g-factor, FMR linewidth at 8 GHz, and net anisotropy of the films in panel (a). The g-factors are close to 2, as expected for Fe^{3+}.**

in-plane compressive strain. LuBiIG and the BiIG/LuIG multilayer are under a smaller compressive strain.

Figure 4b shows that BiIG, LuIG, LuBiIG, and the BiIG/LuIG multilayer all have an in-plane easy axis and M_s = 135 ± 15 kA/m, similar to the bulk magnetization of IGs with nonmagnetic *c*-site ions, including LuIG, YIG, and BiYIG.[31,48] Anisotropy was measured by FMR, Figure 4c and Supplementary Tables S2, S3. All four films have a negative K_{eff} ; however, after subtracting the shape anisotropy, the remaining anisotropy ($K = K_{\mathrm{eff}} - K_{\mathrm{shape}}$) is positive for LuIG and BiIG (i.e., favoring PMA) and negative for LuBiIG and the BiIG/LuIG multilayer. The values of K can be explained by magnetoelastic anisotropy, except in the case of BiIG, which exhibits an additional source of PMA, Supplementary Note 6.

Although the anisotropy and magnetization of the LuBiIG solid solution and the BiIG/LuIG multilayer are similar, their FMR linewidths are dramatically different. The BiIG film and the multilayer both have much greater linewidths (48 and 33 kA/m, respectively, at 8 GHz) compared to LuIG and BiLuIG (1.7 and 5.8 kA/m, respectively). The high linewidths associated with BiIG are likely to be a result of defects in the strained metastable compound.[50,51] The high linewidth of the BiIG/LuIG multilayer is consistent with the presence of BiIG and thus indicates that composition modulation is present within the multilayer film.

CONCLUSIONS

We have demonstrated the synthesis of coherent superlattices of a complex oxide, iron garnet. A composition modulation in the c-site cation can be obtained for a layer thickness of 0.45 nm, less than half of the lattice parameter. Superlattice formation is revealed directly by compositional mapping using both electron microscopy and atom probe tomography and by X-ray diffraction and is inferred from the magnetic properties of the films. In particular, TbIG/TmIG superlattices with layers of 0.45 nm and above show PMA in common with the end-members TmIG and TbIG, dominated by magnetoelastic anisotropy, whereas a solid solution TbTmIG has an in-plane easy axis as a result of its low strain and low magnetostriction. Furthermore, LuIG/BiIG with 2.9 nm layer thickness has a high FMR linewidth, in common with that of the end-member BiIG, whereas the solid solution LuBiIG has a low linewidth.

Oxide heterostructures exhibit a wealth of useful and fascinating physical and electronic properties that emerge from gradients and asymmetry in strain, composition, and charge transfer at interfaces. Much of the research has focused on perovskites; however, the garnet heterostructures demonstrated here provide an even greater range of compositional parameters, resulting from the three different cation sites present in the crystal. The ability to modulate the composition of iron garnets on a sub-unit cell length scale provides opportunities for manipulating the electronic and magnetic properties of an important class of materials with exceptional and tunable magnetic and magneto-optical properties and scope for developing and exploiting interfacial phenomena.

METHODS

Films were grown by pulsed laser deposition on GGG substrates with (111) and (100) orientations and on GSGG substrates with (111) orientation (MTI, Inc.). Commercially available TbIG ($Tb_3Fe_5O_{12}$), TmIG ($Tm_3Fe_5O_{12}$), EuIG ($Eu_3Fe_5O_{12}$), BiIG ($Bi_3Fe_5O_{12}$), and LuIG ($Lu_3Fe_5O_{12}$) targets with purity above 99.9% were used for PLD in a Neocera chamber with a Compex Pro laser of 248 nm wavelength, fluence of 2.0 J/cm^2, repetition rate of 10 Hz, and oxygen partial pressure of 150 mTorr. TbIG, EuIG, and TmIG were deposited in one chamber on substrates heated to 750 °C (heater set point temperature of 900 °C), while a different chamber was used for deposition of BiIG and LuIG with a substrate temperature of 550 °C (heater set point of 700 °C). The deposited films were cooled to room temperature at a rate of 20 °C/min in an oxygen pressure of 150 mTorr. A Bruker D8 Discover instrument was used to perform HRXRD measurements. XRD scans for multilayered films were simulated using LEPTOS. In the simulations, each layer was assumed to be ideally crystalline with the composition of the end-member, and all layers were assumed to be strained in-plane to match the substrate lattice parameter. Interfaces were modeled to have an abrupt composition change from one end-member to the other without any intermixing between layers. Topographical images of the film surface were obtained using an AFM model Cypher S. An ADE 1660 VSM was used to perform magnetic measurements.

The TEM lamella sample was prepared using a VELION FIB-SEM system with a 35 keV Au$^+$ ion beam, followed by ion polishing by Ar$^+$. The HAADF and EDS images were acquired on a Themis Z STEM at 200 keV with a chromatic aberration corrector. Specimen tips for the 3D APT were prepared using an FEI Helios 660 Nanolab Dual-Beam FIB/SEM. Standard APT sample preparation procedures were followed for the lift out: sharpening of the tips was performed first with an ion beam accelerating voltage of 30 kV and then (for final shaping and cleanup) at 2 kV. APT was performed using a Cameca LEAP 4000X HR instrument in laser pulsing mode, with the following operating conditions: laser pulse energy, 20 pJ, repetition rate, 100 kHz; base temperature, 40 K; and detection rate, 1%. Reconstruction and analysis of the data were performed using Cameca IVAS 3.6.14 software. A 1D concentration profile along a cylindrical subvolume parallel to the long axis of the specimen tip was extracted, and then, the ion counts were converted into cation ratios. The accurate oxygen content cannot be determined via APT because the oxygen field evaporates as both O$^+$ and O_2^{+2}, which have the same mass-to-charge ratio. The thickness calibration was obtained from an HRXRD analysis.

FMR[52] measurements were performed to determine the net anisotropy of the films using a broadband FMR system with a coplanar waveguide. An r.f. magnetic field of f = 5 to 17 GHz was applied perpendicular to the film, while an in-plane dc magnetic field was swept from μ_0H = 0 to 0.6 T. The resonance field H_{res} and linewidth ΔH were determined for each frequency by fitting the detected voltage with the derivative of the sum of a symmetric and antisymmetric Lorentzian:[53]

$$P = \frac{\mathrm{d}}{\mathrm{d}H}\left[\frac{S\Delta H^2 + A_s(H - H_{\mathrm{res}})}{4(H - H_{\mathrm{res}})^2 + \Delta H^2}\right] \tag{3}$$

where S and A_s are fitting coefficients. The Lande g-factor and M_{eff} were obtained for all films by fitting the frequency of the magnetic field f and H_{res} to the following equation:[54]

$$f = \frac{g\mu_0\mu_B}{2\pi\hbar}\sqrt{H_{\mathrm{res}}(H_{\mathrm{res}} + M_{\mathrm{eff}})} \tag{4}$$

SMR was measured by first depositing 4 nm Pt on top of the garnet film using RF magnetron sputtering with an Ar pressure of 2 mTorr. The 22 nm thick films show PMA and similar hysteresis to that of the thicker multilayered films but have a root-mean-square roughness below 0.2 nm. The Pt/REIG longitudinal and Hall resistances are measured by wire bonding at the corners of a continuous square film sample in a Van der Pauw–Hall geometry. The magnetic field was applied by a solenoid coil magnet, and the resistance was measured by standard low-frequency lock-in amplifiers. An electric current in the Pt layer produces a spin current perpendicular to the film plane by the spin Hall effect,[55] which interacts with the REIG magnetization and modulates the resistivity of Pt.[56] The transverse Hall resistance is given by

$$R_H = R_H^{\mathrm{SMR}}\sin^2\theta\sin(2\Phi) + R_H^{\mathrm{AHE,SMR}}\cos\theta + R_H^{\mathrm{OHE}}H_z \tag{5}$$

where θ and Φ are the polar and azimuthal angles of the magnetization, respectively. R_H^{SMR}, $R_H^{\mathrm{AHE,\ SMR}}$, and R_H^{OHE} are manifestations of the SMR, anomalous Hall effect-like SMR, and ordinary Hall effect (OHE), respectively, and H_z is the applied out-of-plane magnetic field. For films with PMA, we apply an in-plane magnetic field at 45° to the current direction and measure $H_{\mathrm{K,eff}}$, the field required to saturate R_{H}, using a standard lock-in technique with the Van der Pauw method and fitting the data to a macrospin model.

ASSOCIATED CONTENT

Supporting Information

The Supporting Information is available free of charge at https://pubs.acs.org/doi/10.1021/acsnano.4c11117.

Data tables; anisotropy analysis; and additional data from transmission electron microscopy, atom probe tomography, X-ray diffraction, magnetic hysteresis loops, and ferromagnetic resonance (PDF)

AUTHOR INFORMATION

Corresponding Author

Caroline A. Ross − *Department of Materials Science and Engineering, Massachusetts Institute of Technology, Cambridge, Massachusetts 02139, United States*; orcid.org/0000-0003-2262-1249; Email: caross@mit.edu

Authors

Bharat Khurana − *Department of Materials Science and Engineering, Massachusetts Institute of Technology, Cambridge, Massachusetts 02139, United States*

Allison C. Kaczmarek − *Department of Materials Science and Engineering, Massachusetts Institute of Technology, Cambridge, Massachusetts 02139, United States*

Chung-Tao Chou − *Department of Physics and Department of Electrical Engineering and Computer Science, Massachusetts Institute of Technology, Cambridge, Massachusetts 02139, United States*

Tingyu Su − *Department of Mechanical Engineering, Massachusetts Institute of Technology, Cambridge, Massachusetts 02139, United States*; orcid.org/0000-0002-1154-2855

Katharina Lasinger − *Department of Materials Science and Engineering, Massachusetts Institute of Technology, Cambridge, Massachusetts 02139, United States; Department of Materials, ETH Zurich, CH-8093 Zurich, Switzerland*

Tomas Grossmark − *Department of Materials Science and Engineering, Massachusetts Institute of Technology, Cambridge, Massachusetts 02139, United States*

David C. Bono − *Department of Materials Science and Engineering, Massachusetts Institute of Technology, Cambridge, Massachusetts 02139, United States*

Luqiao Liu − *Department of Electrical Engineering and Computer Science, Massachusetts Institute of Technology, Cambridge, Massachusetts 02139, United States*; orcid.org/0000-0001-6892-8102

Complete contact information is available at: https://pubs.acs.org/10.1021/acsnano.4c11117

Notes

The authors declare no competing financial interest.

ACKNOWLEDGMENTS

Support of the National Science Foundation under award DMR-2323132 is gratefully acknowledged. This work was performed in part using facilities of MIT.nano and in part at the Harvard University Center for Nanoscale Systems (CNS), a member of the National Nanotechnology Coordinated Infrastructure Network (NNCI), which is supported by the National Science Foundation under the NSF award ECCS-2025158. Dr. Austin Akey kindly helped with the APT sample preparation and measurement. C.T.C. and L.L. acknowledge support from National Science Foundation award ECCS-2309838. A.K. acknowledges an NSF Graduate Fellowship.

REFERENCES

(1) Ohtomo, A.; Hwang, H. Y. A High-Mobility Electron Gas at the LaAlO3/SrTiO3 Heterointerface. *Nature* **2004**, *427*, 423−426.

(2) Bousquet, E.; Dawber, M.; Stucki, N.; Lichtensteiger, C.; Hermet, P.; Gariglio, S.; Triscone, J.-M.; Ghosez, P. Improper Ferroelectricity in Perovskite Oxide Artificial Superlattices. *Nature* **2008**, *452*, 732−736.

(3) Murata, T.; Kozuka, Y.; Uchida, M.; Kawasaki, M. Magnetic Properties of Spin Frustrated Spinel ZnFe2O4/ZnCr2O4 Superlattices. *J. Appl. Phys.* **2015**, *118*, 193901.

(4) Kawasaki, J. K.; Baek, D.; Paik, H.; Nair, H. P.; Kourkoutis, L. F.; Schlom, D. G.; Shen, K. M. Rutile IrO2/TiO2 Superlattices: A Hyperconnected Analog to the Ruddelsden-Popper Structure. *Phys. Rev. Mater.* **2018**, *2*, No. 054206.

(5) Adam, J. D.; Collins, J. H. Microwave Magnetostatic Delay Devices Based on Epitaxial Yttrium Iron Garnet. *Proc. IEEE* **1976**, *64*, 794−800.

(6) Bi, L.; Hu, J.; Dionne, G. F.; Kimerling, L.; Ross, C. A. Monolithic Integration of Chalcogenide Glass/Iron Garnet Waveguides and Resonators for on-Chip Nonreciprocal Photonic Devices. In *Integrated Optics: Devices, Materials, and Technologies XV*; SPIE, 2011; Vol. *7941*, pp 28−37.

(7) Yan, W.; Yang, Y.; Yang, W.; Qin, J.; Deng, L.; Bi, L. On-Chip Nonreciprocal Photonic Devices Based on Hybrid Integration of Magneto-Optical Garnet Thin Films on Silicon. *IEEE J. Sel. Top. Quantum Electron.* **2022**, *28*, 6100515.

(8) Lu, J.; Ueda, K.; Yagi, H.; Yanagitani, T.; Akiyama, Y.; Kaminskii, A. A. Neodymium Doped Yttrium Aluminum Garnet (Y3Al5O12) Nanocrystalline Ceramics—a New Generation of Solid State Laser and Optical Materials. *J. Alloys Compd.* **2002**, *341*, 220−225.

(9) Lu, J.; Prabhu, M.; Xu, J.; Ueda, K.; Yagi, H.; Yanagitani, T.; Kaminskii, A. A. Highly Efficient 2% Nd:Yttrium Aluminum Garnet Ceramic Laser. *Appl. Phys. Lett.* **2000**, *77*, 3707−3709.

(10) Cussen, E. J. Structure and Ionic Conductivity in Lithium Garnets. *J. Mater. Chem.* **2010**, *20*, 5167−5173.

(11) Dionne, G. F. *Magnetic Oxides*; Springer: US, Boston, MA, 2009.

(12) Geller, S.; Gilleo, M. A. Structure and Ferrimagnetism of Yttrium and Rare-Earth−Iron Garnets. *Acta Crystallogr.* **1957**, *10*, 239.

(13) Pauthenet, R. Magnetic Properties of the Rare Earth Garnets. *J. Appl. Phys.* **1959**, *30*, S290−S292.

(14) Catalano, S.; Gibert, M.; Fowlie, J.; Íñiguez, J.; Triscone, J.-M.; Kreisel, J. Rare-Earth Nickelates RNiO3: Thin Films and Heterostructures. *Rep. Prog. Phys. Phys. Soc. G. B* **2018**, *81*, No. 046501.

(15) Zhou, Z.; Guo, L.; Yang, H.; Liu, Q.; Ye, F. Hydrothermal Synthesis and Magnetic Properties of Multiferroic Rare-Earth Orthoferrites. *J. Alloys Compd.* **2014**, *538*, 21−31.

(16) Belov, K. P.; Kadomtseva, A. M. Magnetoelastic Properties Of Rare-Earth Orthoferrites. *Sov. Phys. Uspekhi* **1971**, *14*, 154−163.

(17) Vilarinho, R.; Weber, M. C.; Guennou, M.; Miranda, A. C.; Dias, C.; Tavares, P.; Kreisel, J.; Almeida, A.; Moreira, J. A. Magnetostructural Coupling in RFeO3 (R = Nd, Tb, Eu and Gd). *Sci. Rep.* **2022**, *12*, 9697.

(18) Haye, E.; Capon, F.; Barrat, S.; Boulet, P.; André, E.; Carteret, C.; Bruyère, S. Properties of Rare-Earth Orthoferrites Perovskite Driven by Steric Hindrance. *J. Alloys Compd.* **2016**, *657*, 631−638.

(19) Middey, S.; Meyers, D.; Kareev, M.; Moon, E. J.; Gray, B. A.; Liu, X.; Freeland, J. W.; Chakhalian, J. Epitaxial Growth of (111)-Oriented LaAlO3/LaNiO3 Ultra-Thin Superlattices. *Appl. Phys. Lett.* **2012**, *101*, 261602.

(20) Hirai, D.; Matsuno, J.; Takagi, H. Fabrication of (111)-Oriented Ca0.5Sr0.5IrO3/SrTiO3 Superlattices—A Designed Playground for Honeycomb Physics. *APL Mater.* **2015**, *3*, No. 041508.

(21) Panomsuwan, G.; Takai, O.; Saito, N. Epitaxial Growth of (111)-Oriented BaTiO3/SrTiO3 Perovskite Superlattices on Pt(111)/Ti/Al2O3(0001) Substrates. *Appl. Phys. Lett.* **2013**, *103*, 112902.

(22) Yahiro, H.; Tanaka, H.; Yamamoto, Y.; Kawai, T. Construction of ZnFe2O4/ZnGa2O4 Spinel-Type Artificial Superlattice by Pulsed Laser Deposition. *Jpn. J. Appl. Phys.* **2002**, *41*, 5153−5154.

(23) Piamonteze, C.; Gibert, M.; Heidler, J.; Dreiser, J.; Rusponi, S.; Brune, H.; Triscone, J.-M.; Nolting, F.; Staub, U. Interfacial Properties of LaMnO 3/LaNiO 3 Superlattices Grown along (001) and (111) Orientations. *Phys. Rev. B* **2015**, *92*, No. 014426.

(24) Yin, L.; Mi, W.; Wang, X. Prediction of a Metal−Insulator Transition and a Two-Dimensional Electron Gas in Orthoferrite LaTiO3/Tetragonal BiFeO3 Heterostructures. *J. Mater. Chem. C* **2015**, *3*, 11066.

(25) Chen, B.; et al. Spatially Controlled Octahedral Rotations and Metal−Insulator Transitions in Nickelate Superlattices. *Nano Lett.* **2021**, *21*, 1295−1302.

(26) Hwang, J.; Son, J.; Zhang, J. Y.; Janotti, A.; Van de Walle, C. G.; Stemmer, S. Structural Origins of the Properties of Rare Earth Nickelate Superlattices. *Phys. Rev. B* **2013**, *87*, No. 060101.

(27) Boldrin, D.; et al. Giant Piezomagnetism in Mn3NiN. *ACS Appl. Mater. Interfaces* **2018**, *10*, 18863.

(28) Makushko, P.; et al. Flexomagnetism and Vertically Graded Néel Temperature of Antiferromagnetic Cr2O3 Thin Films. *Nat. Commun.* **2022**, *13*, 6745.

(29) Kabychenkov, A. F.; Lisovskii, F. V. Flexomagnetic and Flexoantiferromagnetic Effects in Centrosymmetric Antiferromagnetic Materials. *Technol. Phys.* **2019**, *64*, 980−983.

(30) Rosenberg, E. R.; Litzius, K.; Shaw, J. M.; Riley, G. A.; Beach, G. S. D.; Nembach, H. T.; Ross, C. A. Magnetic Properties and Growth-Induced Anisotropy in Yttrium Thulium Iron Garnet Thin Films. *Adv. Electron. Mater.* **2021**, *7*, No. 2100452.

(31) Fakhrul, T.; Khurana, B.; Nembach, H. T.; Shaw, J. M.; Fan, Y.; Riley, G. A.; Liu, L.; Ross, C. A. Substrate-Dependent Anisotropy and Damping in Epitaxial Bismuth Yttrium Iron Garnet Thin Films. *Adv. Mater. Interfaces* **2023**, *10*, No. 2300217.

(32) Bode, M.; Heide, M.; von Bergmann, K.; Ferriani, P.; Heinze, S.; Bihlmayer, G.; Kubetzka, A.; Pietzsch, O.; Blügel, S.; Wiesendanger, R. Chiral Magnetic Order at Surfaces Driven by Inversion Asymmetry. *Nature* **2007**, *447*, 190−193.

(33) Nur-E-Alam, M.; Vasiliev, M.; Kotov, V.; Alameh, K. Recent Developments in Magneto-Optic Garnet-Type Thin-Film Materials Synthesis. *Procedia Eng.* **2014**, *76*, 61−73.

(34) Kahl, S.; Grishin, A. M. Enhanced Faraday Rotation in All-Garnet Magneto-Optical Photonic Crystal. *Appl. Phys. Lett.* **2004**, *84*, 1438−1440.

(35) Simion, B. M.; Ramesh, R.; Keramidas, V. G.; Thomas, G.; Marinero, E.; Pfeffer, R. L. Magnetic Characterization of Epitaxial Y5FeeO12/Bi3Fe5O12 and Y5Fe3O12/Eu1Bi2Fe5 O12 Heterostructures Grown by Pulsed Laser Deposition. *J. Appl. Phys.* **1994**, *76*, 6287−6289.

(36) Rastogi, A.; Moorthy, V. N. Magnetic Properties of Multilayers of Nano Thin Co,Ce-Doped and Undoped Yttrium Iron Garnet Films for Magneto-Optic Applications. *Mater. Sci. Eng., B* **2002**, *95*, 131−136.

(37) Chern, M. Y.; Fang, C. C.; Liaw, J. S.; Lin, J. G.; Huang, C. Y. Study of Ultrathin Y3Fe5O12/Gd3Ga5O12 Superlattices. *Appl. Phys. Lett.* **1996**, *69*, 854−856.

(38) Chern, M. Y.; Lee, W. S.; Liou, D. R. Curie Temperatures of Y3Fe5O12/Gd3Fe5O12 Superlattices. *J. Magn. Magn. Mater.* **1997**, *170*, L243−L247.

(39) Krockenberger, Y.; Lee, J. S.; Okuyama, D.; Nakao, H.; Murakami, Y.; Kawasaki, M.; Tokura, Y. Garnet Superlattice as a Transparent Above-Room-Temperature Polar Magnet. *Phys. Rev. B* **2011**, *83*, No. 214414.

(40) Lee, C.-H.; Liang, K. S.; Chern, M. Y. The Structures of Yttrium Iron Garnet/Gadolinium Gallium Garnet Superlattice Thin Films Studied by Synchrotron X-Ray Surface Scattering. *J. Chin. Chem. Soc.* **2013**, *60*, 870−876.

(41) Sloyan, K. A.; May-Smith, T. C.; Zervas, M.; Eason, R. W.; Huband, S.; Walker, D.; Thomas, P. A. Growth of Crystalline Garnet Mixed Films, Superlattices and Multilayers for Optical Applications via Shuttered Combinatorial Pulsed Laser Deposition. *Opt. Express* **2010**, *18*, 24679.

(42) Khurana, B.; Bauer, J. J.; Zhang, P.; Safi, T.; Chou, C.-T.; Hou, J. T.; Fakhrul, T.; Fan, Y.; Liu, L.; Ross, C. A. Magnetism and Spin Transport in Platinum/Scandium-Substituted Terbium Iron Garnet Heterostructures. *Phys. Rev. Mater.* **2021**, *5*, No. 084408.

(43) Rosenberg, E. R.; et al. Magnetism and Spin Transport in Rare-Earth-Rich Epitaxial Terbium and Europium Iron Garnet Films. *Phys. Rev. Mater.* **2018**, *2*, No. 094405.

(44) Manuilov, S. A.; Grishin, A. M. Pulsed Laser Deposited Y3Fe5O12 Films: Nature of Magnetic Anisotropy II. *J. Appl. Phys.* **2010**, *108*, No. 013902.

(45) Kaczmarek, A.; et al. Atomic order of rare earth ions in a complex oxide: a path to magnetotaxial anisotropy. *Nat. Commun.* **2024**, *15*, 5053.

(46) Yi, D.; Amari, H.; Balakrishnan, P. P.; Klewe, C.; N'Diaye, A. T.; Shafer, P.; Browning, N.; Suzuki, Y. Enhanced Interface-Driven Perpendicular Magnetic Anisotropy by Symmetry Control in Oxide Superlattices. *Phys. Rev. Appl.* **2021**, *15*, No. 024001.

(47) Lazenka, V.; Jochum, J.; Lorenz, M.; Modarresi, H.; Gunnlaugsson, H.; Grundmann, M.; Van Bael, M.; Temst, K.; Vantomme, A. Interface Induced Out-of-Plane Magnetic Anisotropy in Magnetoelectric BiFeO 3 -BaTiO 3 Superlattices. *Appl. Phys. Lett.* **2017**, *110*, No. 092902.

(48) Hellwege, K.-H.; Hellwege, A. M., Eds., *Part A: Garnets and Perovskites*; Springer-Verlag: Berlin/Heidelberg, 1978; Vol. *12a*.

(49) Tepper, T.; Ross, C. A. Pulsed Laser Deposition and Refractive Index Measurement of Fully Substituted Bismuth Iron Garnet Films. *J. Cryst. Growth* **2003**, *255*, 324−331.

(50) Sun, Y.; Song, Y.-Y.; Chang, H.; Kabatek, M.; Jantz, M.; Schneider, W.; Wu, M.; Schultheiss, H.; Hoffmann, A. Growth and Ferromagnetic Resonance Properties of Nanometer-Thick Yttrium Iron Garnet Films. *Appl. Phys. Lett.* **2012**, *101*, 152405.

(51) Sharma, V.; Kumari, S.; Kuanr, B. K. Rare Earth Doped M-Type Hexaferrites; Ferromagnetic Resonance and Magnetization Dynamics. *AIP Adv.* **2018**, *8*, No. 056232.

(52) Zhang, L.; Zhang, D.; Jin, L.; Liu, B.; Meng, H.; Tang, X.; Li, M.; Liu, S.; Zhong, Z.; Zhang, H. Fabrication and Broadband Ferromagnetic Resonance Studies of Freestanding Polycrystalline Yttrium Iron Garnet Thin Films. *APL Mater.* **2021**, *9*, No. 061105.

(53) Gonzalez-Fuentes, C.; Dumas, R. K.; García, C. Systematic Errors in the Determination of the Spectroscopic G-Factor in Broadband Ferromagnetic Resonance Spectroscopy: A Proposed Solution. *J. Appl. Phys.* **2018**, *123*, No. 023901.

(54) Shaw, J. M.; Nembach, H. T.; Silva, T. J. Measurement of Orbital Asymmetry and Strain in Co90Fe10/Ni Multilayers and Alloys: Origins of Perpendicular Anisotropy. *Phys. Rev. B* **2013**, *87*, No. 054416.

(55) Hirsch, J. E. Spin Hall Effect. *Phys. Rev. Lett.* **1999**, *83*, 1834−1837.

(56) Chen, Y.-T.; Takahashi, S.; Nakayama, H.; Althammer, M.; Goennenwein, S. T. B.; Saitoh, E.; Bauer, G. E. W. Theory of Spin Hall Magnetoresistance. *Phys. Rev. B* **2013**, *87*, No. 144411.